Ocean Engineering 236 (2021) 109508

Contents lists available at ScienceDirect

Ocean Engineering

journal homepage: www.elsevier.com/locate/oceaneng

Prediction of deepwater riser VIV with an improved time domain model including non-linear structural behavior

Sang Woo Kim [a,*], Svein Sævik [a], Jie Wu [b], Bernt Johan Leira [a]

[a] Department of Marine Technology, Norwegian University of Science and Technology (NTNU), 7491, Trondheim, Norway
[b] SINTEF Ocean, 7052 Trondheim, Norway

ARTICLE INFO

Keywords:
Vortex-induced vibration
Large-scale experiment
Synchronization
Time-sharing process
Sheared current

ABSTRACT

In this paper, vortex-induced vibrations (VIV) of deepwater risers including the VIV-induced tension fluctuations were simulated using a time domain VIV model. Data from a large-scale riser experiment was applied for correlation studies. As a first step, a new combination of in-line and cross-flow synchronization models with empirical parameters was proposed for better in-line response prediction. The performance of the improved load model was investigated based on a linear riser model. The results showed that the in-line response and its synchronization pattern were improved compared to the previous load model. Then, the improved load model was combined with a non-linear structural riser model to explore the effect of tension fluctuations. As observed in the tests, simulations showed that the tension fluctuations influenced the stability of VIV and possibly decreased the resulting vibration amplitudes. Lastly, the VIV prediction performance of the load model was evaluated with respect to frequency contents, stress levels, and fatigue damage. From the results, it was found that the improved load model in combination with the non-linear structural model reflected the response characteristics observed in the tests.

1. Introduction

For a bluff body subjected to fluid flow, vortices are formed in the wake and cause alternating lift and drag forces. When the vortex shedding frequency becomes close to the eigenfrequencies of the body resulting in strong vibrations, and this is referred to as Vortex-Induced Vibration (VIV). VIV causes fast accumulations of fatigue damages to marine risers due to a high-frequency response. There have been attempts to explore the physics of VIV for several decades, and it is revealed that VIV is influenced by a large number of parameters. Relevant studies and findings were summarized by Sarpkaya (2004), Williamson and Govardhan (2004) and Gabbai and Benaroya (2005) based on short rigid cylinder test data.

Moreover, several long flexible pipe tests have been conducted to unveil characteristics of deepwater riser VIV. Considering only tests with an aspect ratio (= Length/Diameter, L/D) above 1000, the first large scale riser test was performed in Hanøytangen, Norway (L/D: 3000) (Huse, 1997; Baarholm et al., 2006; Lie and Kaasen, 2006). MIT research teams also conducted field tests of long flexible pipes in Lake Seneca (L/D: 3671) and Gulf stream (L/D: 4198), USA (Vandiver et al., 2006, 2009). Furthermore, the Norwegian Deepwater Programme (NDP) carried out a high mode VIV test in MARINTEK's Ocean Basin (L/D: 1407) (Trim et al., 2005; Braaten and Lie, 2005). Based on the test results, the features of long flexible pipes VIV were summarized (Voie et al., 2016). A key feature of long flexible riser VIV, is the multi-mode response due to the variable current throughout the water column. Multi-mode VIV responses in terms of amplitude and frequency may vary along the pipe and with time even under a stationary flow due to its instability (Larsen et al., 2012). As a result of the high aspect ratio, the mode order of cross-flow (CF) vibrations may be relative high, with traveling waves observed for mode orders exceeding about 10. The dynamic tension variations by the VIV responses will be more significant for increasing flow speed and response mode orders even though the test setup is designed to minimize it. There is generally a lack of understanding of how such structural non-linearity can influence the VIV process at high response mode orders.

Semi-empirical frequency domain models have been used by the industry. VIVANA (Larsen et al., 2017), Shear7 (Vandiver and Li, 2005), and VIVA (Triantafyllou et al., 1999) are representative methods for this approach. All methods are based on hydrodynamic coefficients related to the flow velocity, cross-section parameters, and the predicted response. VIV response is solved in the frequency domain based on a linear structural model, which represents a fundamental limitation with respect to describing non-stationary VIV responses and non-linear structural phenomena such as tension variation. Furthermore, in order

* Corresponding author.
E-mail address: sangwoo.kim@ntnu.no (S.W. Kim).

https://doi.org/10.1016/j.oceaneng.2021.109508
Received 6 November 2020; Received in revised form 8 July 2021; Accepted 12 July 2021
Available online 21 July 2021

to describe the frequency and response variation in time and space, two idealized concepts are introduced in some of these tools. The space-sharing concept (or concurrent frequency) was developed to describe the frequency competition in a sheared flow with multiple response frequencies. While, the time-sharing concept (or consecutive frequencies), was proposed by Swithenbank (2007) to explain the frequency variation in time. However, these concepts are approximations of the true physical process. The Computational Fluid Dynamics (CFD) methods can provide alternative solutions. However, CFD methods are requiring extensive computing resources, and they are hence not suitable for design purposes. As a result of the complexity in response behavior and the difficulties in developing engineering models that can capture the inherent physics, a high safety factor is demanded in the design of deepwater risers against VIV loads (DNV.GL, 2017). Therefore, there is a need for developing more accurate VIV prediction tools for deepwater riser systems.

As an alternative, different time domain VIV models have been proposed, including wake oscillator and semi-empirical models, and the models can account for structural non-linearities and time-varying flow conditions. The wake oscillator models are normally based on the Van der Pol equation in order to describe the wake and vortex shedding. Several wake oscillator models have been proposed in order to simulate two degrees-of-freedom VIV, however, it has been found difficult to determine empirical parameters that can cover both free and forced oscillation tests (Facchinetti et al., 2004; Ogink and Metrikine, 2010; Srinil and Zanganeh, 2012). For the semi-empirical time domain models, the vortex shedding forces are formulated by the utilization of empirical parameters. A time domain coupled model of cross-flow and in-line (IL) was proposed (Xue et al., 2015; Yuan et al., 2017). The vortex shedding forces were formulated by the hydrodynamic coefficients being dependent on the non-dimensional amplitude and frequency. However, the degree of validation of this model was limited.

Another semi-empirical time domain model for the cross-flow load was introduced by Thorsen et al. (2014) which later was implemented as an additional load term to the classical Morison's equation (Thorsen et al., 2016, 2017). Basically, the VIV load term consists of a vortex shedding force coefficient and a synchronization model, where the vortex shedding force coefficient determines the magnitude of the vortex shedding force. A synchronization model has been introduced to model the phase difference between the instantaneous relative flow velocity and the vortex shedding forces in a local co-ordinate system. The initial cross-flow load model has been systematically validated against a variety of model test data (Wu et al., 2020a). Subsequently, the load model was updated in order to include the in-line terms (Ulveseter et al., 2018, 2019). The cross-flow and in-line coupled load model was tested for several flexible pipe experiments in a uniform current (Ulveseter et al., 2019). The empirical parameters were obtained based on rigid cylinder tests with combined IL and CF motion. Furthermore, additional optimization of the coefficients was also performed in relation to sheared current condition by Drengsrud (2019).

As a step of further validation of this time domain VIV model for high mode VIV responses of deepwater riser systems, additional verification was performed with respect to the Hanøytangen experiment (Kim et al., 2021). The two most recently updated and optimized parameter sets by Ulveseter et al. (2018) and Drengsrud (2019) were applied to investigate the correlations between simulation and experiment. Although one of the parameter sets showed a relatively good correlation with the experiments, problems were encountered in relation to particularly two aspects. First of all, predictions for the in-line stresses were inaccurate, and the frequency variation in time of the in-line response was more narrow than the test data. Furthermore, the linear structural model of the Hanøytangen riser model was not adequate in order to represent the present experimental set-up for the high flow speed cases where the tension variations became significant. The tension variations were due to the VIV and the boundary conditions of the Hanøytangen riser model (Huse, 1998, 1999; Huse et al., 1999).

Table 1
Key data for the Hanøytangen riser model.

Parameters	Unit	Value
Length, L	m	90
Outer diameter, D_e	m	0.03
Inner diameter, D_i	m	0.026
Bending stiffness, EI	Nm^2	3639
Mass per unit length, m	kg/m	2.27
Towing velocity, U	m/s	0.38–1.96
Mean of low pretensions, T_{low}	N	1850
Mean of high pretensions, T_{high}	N	3750

By applying the Hanøytangen test data as a basis for validation, the main objective of the present study was to improve the time domain load VIV model with respect to making it more suitable for deepwater riser VIV prediction. Another main objective was to explore the effect of including the non-linear structural features reflected in the actual experimental test set-up. In Section 2, a detailed review of the test and non-linearities embedded in the test are given. In Section 3, the linear and non-linear structural modeling procedures applied for the test set-up are explained. The theoretical background for the previous and new time domain VIV model is reviewed in Section 4. The empirical parameter sets for the previous and proposed load models are summarized in the same section. In Section 5, the prediction performances of different in-line load models and parameter sets are compared based on a linear structural model. The load model that was found to provide the best correlation with the test results was then used to explore the effects of the test set-up structural non-linearities as included in Section 6. The prediction accuracy of the improved load model and the non-linear structural model is summarized in Section 7. The main observations and conclusions are discussed in Section 8.

2. Large scale model test of deepwater riser

2.1. Descriptions of the Hanøytangen experiment

The main purpose of the test was to investigate the high mode VIV responses of a riser in a linearly sheared current condition. In the test, the riser was towed by a vessel along the floating quay, and transducers that were installed on the riser at every 3 m were measuring bi-directional bending strains. In order to expose the riser to a linearly sheared current, the bottom end of the riser was kept tensioned using the buoyancy arrangements. The magnitude of pretension in each test was controlled by the number of buoyancy tanks and the amount of water inside the tanks. The pretensions were divided into low- and high pretension. The detailed set-up of the tests is illustrated in Fig. 1a, and the main data of the Hanøytangen riser model are summarized in Table 1. When it comes to the test procedure, the towing started 25 m west of the center and ended at the opposite side in each test. The location where the riser stood upright over the pulley was designated as the center. The towing was not stable until reaching the designated velocity due to the acceleration at the early phase of the towing. The test procedure is illustrated in Fig. 1b.

2.2. Non-linearities caused by the test set-up

Due to the test set-up, non-linear effects were inevitably observed in the measurements. The main non-linearities associated with the test set-up are classified as:

- The low-frequency components of the vessel motion and buoyancy arrangements (below 1 Hz)
- The friction between the pulley and rope system (± 3 % of the pretension)
- Axial vibrations of the riser due to the cross-flow and in-line vibrations (2ω and 4ω vibrations)

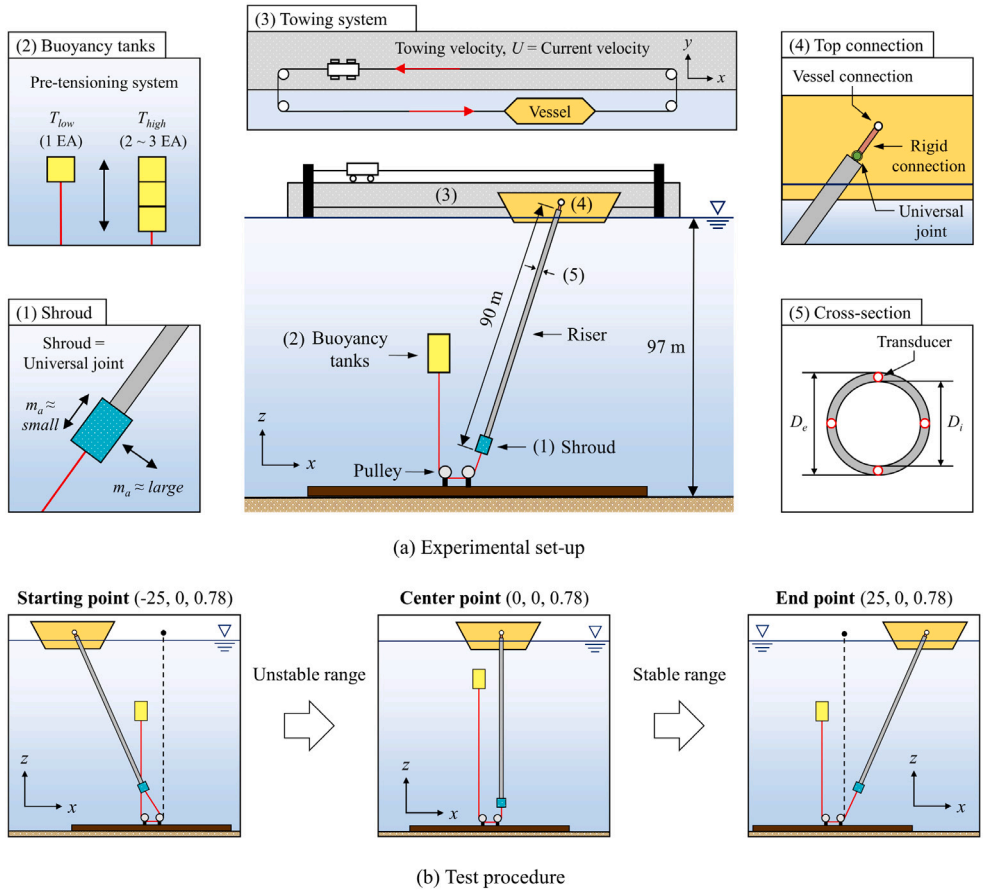

Fig. 1. Set-up and test procedure for the Hanøytangen experiment.

Among these, the VIV induced tension fluctuations at the top of the riser were significant as the current speed increased as discussed in Section 6. Moreover, some of the tests were excluded from the analysis due to large waves during the test and significant deviations of measurements. When the towing speed was low, the VIV was dominated by low-frequent vessel motion, and these tests were excluded in the present study. Accordingly, the number of tests analyzed in this study was 32 out of the 60. Two pre-tension levels were applied in the test and the number of tests in each pretension group was 14 (T_{low}) and 18 (T_{high}), respectively.

3. Numerical modeling of the Hanøytangen test

The Hanøytangen riser model was numerically modeled in RIFLEX (SINTEF Ocean, 2017a), which is based on the 3-D finite element method (FEM). The hydrodynamic bodies related to the towing procedure were modeled in the computer program SIMO (SINTEF Ocean, 2017c), which is developed for simulation of motions and station-keeping behavior of floating bodies. RIFLEX-SIMO coupled simulations were implemented by means of the integrated software SIMA (SINTEF Ocean, 2017b).

3.1. Simplified and advanced modeling methods for the Hanøytangen riser model

The Hanøytangen riser model was modeled in two ways, i.e. by means of a linear structural model with simplified boundary conditions and an non-linear structural model which includes non-linear aspects of the test set-up. Regarding the former, the main simplifications is related to neglecting the vessel and buoyancy arrangements and assuming a constant tension. At the bottom end of the riser, all translations and torsional degrees-of-freedom were kept fixed while the bending moments were free. Furthermore, the pretension in the test was replaced with constant tension at the top of the riser, applying same boundary conditions as in the bottom, except for the free vertical motion. In addition, the current load was modeled as a stationary and linearly sheared current. This riser modeling method is hereafter referred to as a simplified riser model, and its schematic is shown in Fig. 2a.

For the non-linear structural model, the buoyancy arrangements (buoyancy, connecting rope, and pulley) were connected to the bottom end of the riser. However, the pulleys just played the role of changing the direction of the load vector, and it was not possible to model the friction between the pulley and connection rope due to software limitations. The buoyancy was modeled as a floating body where the mass and volumetric displacement of buoyancy were adjusted in each test. The drag coefficients were roughly estimated by referring to Baker et al. (1983), and the added mass coefficients were set to be 1.0 in all directions. Also, universal joints were applied at both ends of the riser, and a shroud attached at the bottom part. Furthermore, a prescribed motion was applied at the vessel end where the towing speed was gradually increased until its stationary value characteristic for each simulation. When the riser passed the center point while keeping a static equilibrium configuration, towing was regarded as stable and ended at 25 m east from the center point. This riser modeling procedure is hereafter referred to as an advanced riser model. The details of the advanced riser model are illustrated in Fig. 2b, and the detailed input parameters for the model are summarized in Table 2.

3.2. Numerical input parameters and post processing of signal

The element numbers and time step size for the simulations were set based on the estimation of the highest possible VIV response frequency,

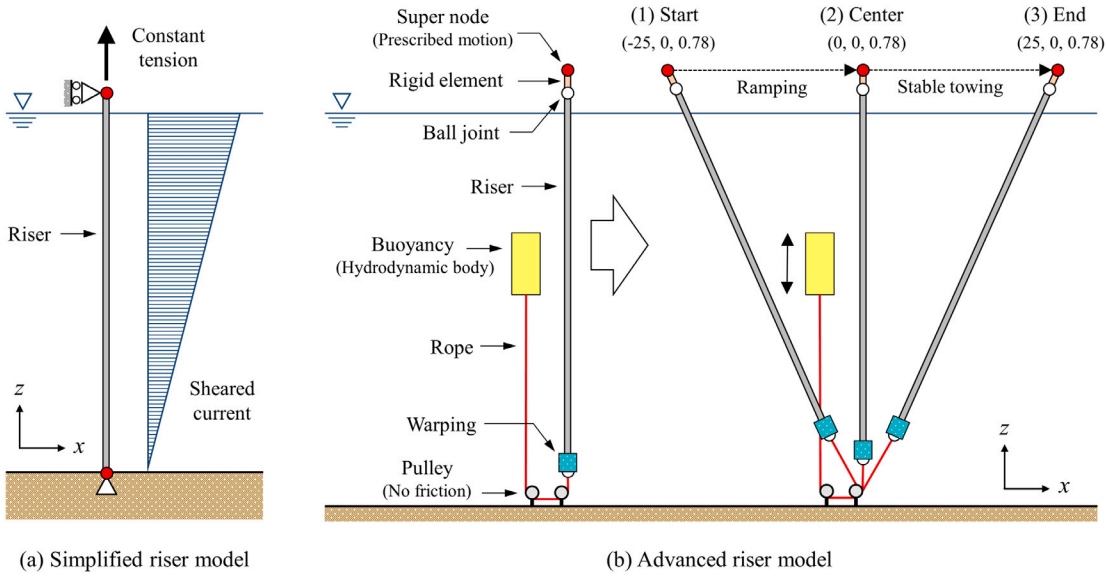

Fig. 2. Illustration of numerical riser models and the simulation procedure.

Table 2
Structural and hydrodynamic data for the advanced riser model.

Parameters	Unit	Value
Buoyancy		
Volumetric displacement for T_{low}	m^3	0.101
Volumetric displacement for T_{high}	m^3	0.327
Drag coefficient in surge direction	–	1.2
Drag coefficient in sway direction	–	1.2
Drag coefficient in heave direction	–	0.8
Added mass coefficient in surge	–	1.0
Added mass coefficient in sway	–	1.0
Added mass coefficient in heave	–	1.0
Connecting rope		
Axial stiffness	kN	640
Length	m	100
Shroud		
Length	m	0.85
Diameter	m	0.5
Added mass in normal direction	kg/m	300
Added mass in tangential direction	kg/m	10

Table 3
Numerical input parameters and filtering ranges.

Parameters	Value
Maximum CF mode number, n_{max}	42
Number of elements ($n_{max} \times 50$)	2100
Number of time steps per CF period	60
Structural damping ratio, ζ	0.3%
Filtering bandwidths (Bending moments)	1.0 Hz–2f_v Hz
Filtering bandwidths (Tension)	1.0 Hz–5f_v Hz

f_v (= StU_{max}/D_e), and the Strouhal number, St, was set to 0.17. The cross-flow mode number was estimated by referring to the tensioned beam theory (Baarholm et al., 2006). Structural damping of the riser was assumed proportional to the system stiffness, i.e. $\mathbf{C} = \alpha_2\mathbf{K}$, where $\mathbf{C}$ and $\mathbf{K}$ are the global damping and stiffness matrices. α_2 was set corresponding to a damping ratio of 0.3% at the frequency, f_v, for each test.

In order to exclude the low frequencies, i.e. motions induced by the vessel and the buoyancy arrangements, the low frequencies below 1 Hz were filtered out for the bending moment and tension signals. Furthermore, for the bending moments, the upper bound of the frequency was set to be twice the shedding frequency, f_v, in order to exclude higher order VIV, i.e. 3ω and 4ω, and it was applied to both the tests and simulations. Regarding the tension signal, a very broad filtering range was applied in order to involve the high-frequency tension fluctuations. The numerical simulation input parameters and filtering range are summarized in Table 3.

For the test data, the relatively stable time series were extracted from the stable towing range for each case. Especially, the section of the signal corresponding to when the vessel was close to the center point was preferred. This is because, as the vessel approaches the end point, the inclination angle of the riser was increasing, resulting in a decreasing mean tension and a variation of the hydrodynamic coefficients. Extracted signals included roughly 150 to 200 steady-state cross-flow periods. Even though the length of the time window was short, it was valid for observing the VIV responses (Larsen et al., 2012). Examples of tension and bending moment signals corresponding to the time window are illustrated in Fig. 3. The same time window as applied for each experiment was applied to extract the results from the advanced riser model simulations. For the simplified riser model, the time window was set to include 200 steady-state cross-flow periods.

4. Time domain VIV model

4.1. Hydrodynamic load model

The time domain VIV model is based on strip theory. The load model is formulated in terms of the incoming flow vectors, the cylinder response vectors, and the hydrodynamic coefficients. The vectors and local coordinate systems of a cylinder in the flow are illustrated in Fig. 4. The incoming flow vector at any cylinder cross-section, $\mathbf{u}$ can be decomposed into a normal- (subscript, n) and a tangential component (subscript, t) to the cylinder strip. Only considering the normal components of the flow, $\mathbf{u}_n$, the interaction between hydrodynamic loads and structure response, $\mathbf{x}_n$ can be simplified into a two-dimensional problem in the cylinder plane, i.e. the $\mathbf{j_1}\mathbf{j_2}$-plane ($\mathbf{j_3}$ is the unit vector in the axial direction of the cylinder). The vortex shedding forces and drag force follow a local axis system where the horizontal axis is parallel to the relative flow velocity vector, $\mathbf{v}_n = \mathbf{u}_n - \dot{\mathbf{x}}_n$. The direction of the vortex shedding forces will be changing as the relative flow changes, however, local cross-flow and in-line directions will be systematically referred to as cross-flow and in-line in the present study. Based on these

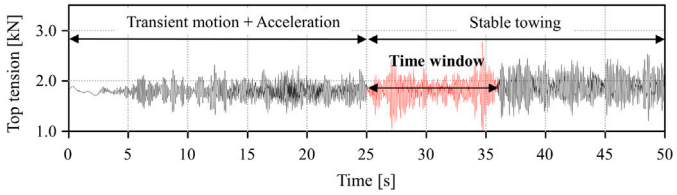

(a) Tension signal at the top of the riser

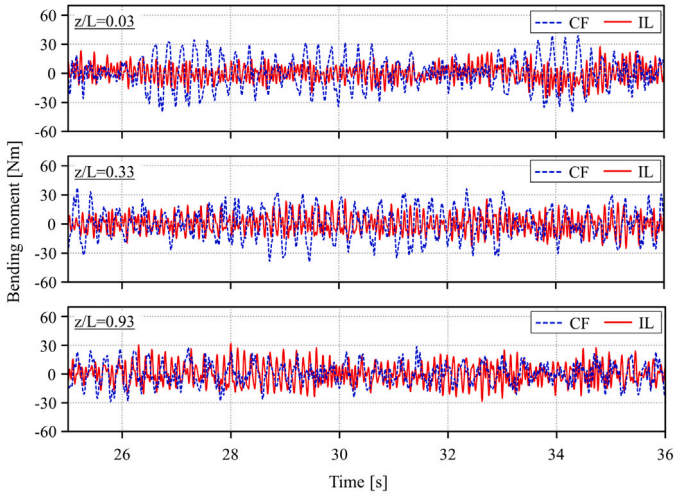

(b) Bending moment signals by applying a time window

Fig. 3. Raw signals for top tension and bending moments ($U = 0.98$ m/s, T_{low}).

definitions, the hydrodynamic loads acting on a cylinder strip (per unit length) is expressed in Eq. (1) by Ulveseter et al. (2018):

$$\mathbf{F}_n = \underbrace{\underbrace{C_M \rho \frac{\pi D_e^2}{4}\dot{\mathbf{u}}_n}_{\text{Froude–Kriloff force}} \underbrace{-(C_M-1)\rho\frac{\pi D_e^2}{4}\ddot{\mathbf{x}}_n}_{\text{Added mass force}} + \underbrace{\frac{1}{2}\rho D_e C_D |\mathbf{v}_n|\mathbf{v}_n}_{\text{Drag force } (\mathbf{F}_{v,x})}}_{\text{Morison's equation}} + \underbrace{\underbrace{\frac{1}{2}\rho D_e C_{v,x}|\mathbf{v}_n|\mathbf{v}_n\cos\phi_{\text{exc},x}}_{\text{In–line vortex shedding force } (\mathbf{F}_{v,x})} + \underbrace{\frac{1}{2}\rho D_e C_{v,y}|\mathbf{v}_n|(\mathbf{j}_3\times\mathbf{v}_n)\cos\phi_{\text{exc},y}}_{\text{Cross–flow vortex shedding force } (\mathbf{F}_{v,y})}}_{\text{Vortex shedding force terms}} \quad (1)$$

where, the first three terms are well known terms from Morison's equation, and C_M, C_D, D_e, and ρ are the inertia coefficient, drag coefficient, cylinder diameter, and fluid density. The remaining two terms are the in-line and cross-flow vortex shedding force. $C_{v,x}$ and $C_{v,y}$ are in-line and cross-flow vortex shedding force coefficients; $\phi_{\text{exc},x}$ and $\phi_{\text{exc},y}$ are the in-line and cross-flow instantaneous phases of the vortex shedding forces.

The load model was intended to be expressed as simply as possible while still including the main VIV physics. Regardless of the frequency or amplitude of VIV, the hydrodynamic coefficients (i.e. C_M, C_D, $C_{v,x}$, and $C_{v,y}$) were assumed constant within the Reynolds number range of the present study. Therefore, the Reynolds number must be accounted for when applying specific coefficients to another case. This approach excludes consideration of the Reynolds number effect, which is still an area of research, see Potts et al. (2018).

4.2. Cross-flow and in-line synchronization

The magnitude of the vortex shedding forces calculated from the Eq. (1) is determined by the coefficients, $C_{v,x}$ and $C_{v,y}$. At the same time, the oscillation of the forces is implemented by the time-varying instantaneous phases, $\phi_{\text{exc},x}$ and $\phi_{\text{exc},y}$. To simulate the lock-in process

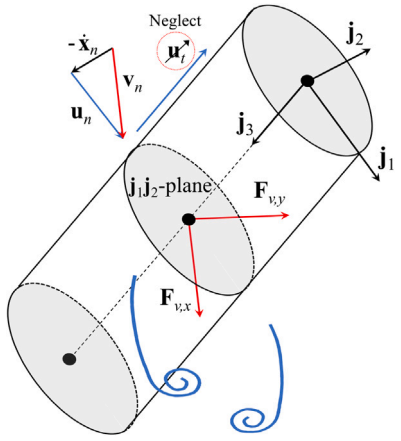

Fig. 4. A cylinder strip with the relevant vectors and local coordinate system.

associated with VIV, synchronization models are applied to each direction ensuring that the instantaneous frequency of the vortex shedding force can increase or decrease so that its phase can match the phase of the instantaneous phase of the cylinder velocity. The synchronization is limited to happen only in the non-dimensional frequency range (i.e. the synchronization range). In the case of cross-flow, the instantaneous frequency of the cross-flow can be formulated as Eqs. (2) and (3) (Thorsen et al., 2017).

$$\frac{d\phi_{\text{exc},y}}{dt} = 2\pi f_{\text{exc},y} = \frac{2\pi|\mathbf{v}_n|}{D_e}\hat{f}_{\text{exc},y} \quad (2)$$

$$\hat{f}_{\text{exc},y} = \begin{cases} \hat{f}_{0,y} + (\hat{f}_{\max,y} - \hat{f}_{0,y})\sin\theta_y, & \theta_y \geq 0 \\ \hat{f}_{0,y} + (\hat{f}_{0,y} - \hat{f}_{\min,y})\sin\theta_y, & \theta_y < 0 \end{cases} \quad (3)$$

where, $\hat{f}_{\min,y}$, $\hat{f}_{\max,y}$, and $\hat{f}_{0,y}$ determine the cross-flow synchronization range and the non-dimensional frequency of maximum energy transfer.

θ_y is the phase difference between the cylinder cross-flow velocity, $\phi_{\dot{y}_{\text{rel}}}$ and the cross-flow vortex shedding force, $\phi_{\text{exc},y}$, i.e $\theta_y = \phi_{\dot{y}_{\text{rel}}} - \phi_{\text{exc},y}$.

Based on Eqs. (2) and (3), synchronization of the cross-flow occurs in the range between $\hat{f}_{\min,y}$ and $\hat{f}_{\max,y}$, and the instantaneous phase of the cross-flow vortex shedding force, $\phi_{\text{exc},y}$ is to be in phase with the cylinder cross-flow velocity at the frequency, $\hat{f}_{0,y}$ (i.e. $\phi_{\dot{y}_{\text{rel}}} = \phi_{\text{exc},y}$). When it comes to the in-line vibration, there are two types of in-line responses. One is the pure in-line response, which takes place at low current speed. Another is the in-line response induced by the cross-flow response, and this is of main interest in this study. For the in-line response induced by the cross-flow response, the experimental observations showed that the in-line vortex shedding frequency is about twice that of the cross-flow vortex shedding (Dahl et al., 2010). The cross-flow dependent in-line synchronization was suggested by Ulveseter et al. (2018):

$$\frac{d\phi_{\text{exc},x}}{dt} = 2\pi \frac{d\phi_{\text{exc},y}}{dt}[1 + \alpha \sin(\phi_{\dot{x}_{\text{rel}}} - \phi_{\text{exc},x})] \tag{4}$$

where, $\phi_{\dot{x}_{\text{rel}}}$ is the instantaneous phase of the local in-line velocity of the cylinder, and α indicates how much the frequency of the in-line force depends on that of the cross-flow force. When α is zero, $d\phi_{\text{exc},x}/dt = 2d\phi_{\text{exc},y}/dt$.

4.3. Self-limiting process and drag amplification

The synchronization concept makes it possible to simulate the self-limiting process using the load model. In the excitation region defined by $\hat{f}_{\min,y}$ and $\hat{f}_{\max,y}$, the phase of the vortex shedding force is close to the phase of the relative velocity of the cylinder. This means that the component of the vortex shedding force in phase with the velocity will provide positive energy to the structural response. The out-of-phase force component becomes the inertia force. The center of the synchronization is determined by the $\hat{f}_{0,y}$ value, around which most of the force is in phase with the velocity. At the same time, the damping force is created by the drag load term, which increases with motion amplitude. The combination of these force terms determines the response as a self-limiting process. Furthermore, the inertia force consists of an out-of-phase component of the vortex shedding force and the additional added mass term in Morison's equation, refer to Eq (1).

Besides, the drag amplification can be described. The drag amplification refers to increased drag forces due to the cross-flow responses compared to that of a fixed cylinder. This is accounted for by the projected force in the global incoming flow direction arising from the vortex shedding force term in Eq. (1). This means that the drag force term in Eq. (1) defines the initial static deformation in the in-line direction. In addition, the deformation will be further increased in the dynamic analysis when the vortex shedding force is activated.

4.4. Improvement of in-line vortex shedding term

The motivation for the load model update was inaccurate in-line predictions while applying the previous time domain VIV model for the Hanøytangen test (Kim et al., 2021). The previous model was based on an in-line synchronization model that was linked to the cross-flow synchronization model (Ulveseter et al., 2019). In an effort to improve the in-line predictions, a new combination of in-line and cross-flow load models with separate synchronization models is introduced.

4.4.1. Independent synchronization of in-line vortex shedding force

The in-line synchronization model in the previous section had been tested and validated for the NDP-high mode VIV tests (Ulveseter et al., 2019; Drengsrud, 2019). However, it was still questionable with respect to the in-line synchronization depending on the cross-flow synchronization. A coupled motion of the cross-flow and in-line oscillation is a result of the dual resonance (Dahl et al., 2010), and the resonances in each direction are independent of each other according to the respective natural frequencies in the two directions. To implement this feature, the principle for cross-flow synchronization was set to be the same as the previous one (i.e Eqs. (2) and (3)) whereas a new in-line synchronization formulation as expressed by Eqs. (5) and (6) is proposed for simultaneous cross-flow and in-line vibrations. This model is basically the same model as proposed by Ulveseter for pure in-line vibration of pipeline free-spans (Ulveseter et al., 2017). The idea adopted here is to apply the same approach for the in-line force component related to cross-flow VIV. Then in principle, by applying a sufficiently wide synchronization range, both pure in-line and combined cross-flow and in-line vibrations can be captured by the same synchronization model.

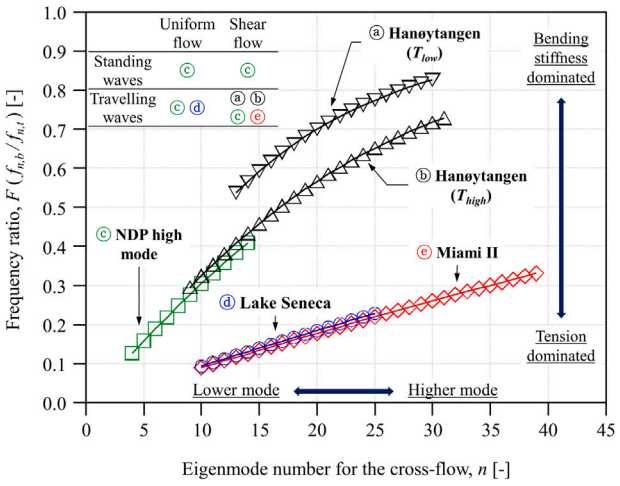

Fig. 5. Comparison of VIV response characteristics for different deepwater riser tests.

$$\frac{d\phi_{\text{exc},x}}{dt} = 2\pi f_{\text{exc},x} = \frac{2\pi |\mathbf{v}_n|}{D_e} \hat{f}_{\text{exc},x} \tag{5}$$

$$\hat{f}_{\text{exc},x} = \begin{cases} \hat{f}_{0,x} + (\hat{f}_{\max,x} - \hat{f}_{0,x}) \sin\theta_x, & \theta_x \geq 0 \\ \hat{f}_{0,x} + (\hat{f}_{0,x} - \hat{f}_{\min,x}) \sin\theta_x, & \theta_x < 0 \end{cases} \tag{6}$$

where, $\hat{f}_{\min,x}$, $\hat{f}_{\max,x}$, and $\hat{f}_{0,x}$ determines the in-line synchronization range and the non-dimensional frequency of maximum energy transfer. θ_x is the phase difference between the cylinder in-line velocity, $\phi_{\dot{x}_{\text{rel}}}$ and the in-line vortex shedding force, $\phi_{\text{exc},x}$, i.e $\theta_x = \phi_{\dot{x}_{\text{rel}}} - \phi_{\text{exc},x}$.

4.4.2. In-line synchronization parameters

To define the proper in-line synchronization ranges, information about the VIV response characteristics of the Hanøytangen riser model was required. A comparison of VIV response characteristics for different deepwater riser tests is provided in Fig. 5. The x-axis gives the cross-flow mode number, n, and the y-axis gives the bending stiffness ratio, F (= $f_{n,b}/f_{n,t}$) which is used to quantify the relative contribution of the bending stiffness to the total stiffness. The test risers models can be modeled as a tensioned beam, and the corresponding eigenfrequencies are given by the following equations:

$$Tensioned\,beam: f_{n,t} = \sqrt{f_{n,s}^2 + f_{n,b}^2} \tag{7}$$

$$Tensioned\,string: f_{n,s} = \frac{n}{2L}\sqrt{\frac{T}{m}} \tag{8}$$

$$Untensioned\,beam: f_{n,b} = \frac{\pi n^2}{2L^2}\sqrt{\frac{EI}{m}} \tag{9}$$

As seen in Fig. 5, for the Hanøytangen riser model, VIV response mode order was relatively high, and the stiffness of the structure was highly dominated by the bending stiffness compared to the same VIV mode order as for Miami II and Lake Seneca. In addition, due to the shear flow condition, the space-sharing and time-sharing processes

Table 4
Empirical parameters of the previous and new time domain VIV models.

Parameters	Prev	New1 (NB)	New2 (WB)
C_D	1.2	1.2	1.2
C_M	2.0	2.0	2.0
$C_{v,y}$	0.85	0.85	0.85
$C_{v,x}$	0.75	0.75	0.75
$\hat{f}_{0,y}$	0.144	0.144	0.144
$\hat{f}_{\min,y}$	0.08	0.08	0.08
$\hat{f}_{\max,y}$	0.208	0.208	0.208
α	0.15	–	–
$\hat{f}_{0,x}$	–	0.288	0.5
$\hat{f}_{\min,x}$	–	0.16	0.1
$\hat{f}_{\max,x}$	–	0.416	0.7

associated with VIV are both likely to be extensive. This implies that the VIV responses can be more unstable than other high mode riser model tests (Wu et al., 2019, 2020b). To satisfy the test conditions, one of the solutions would be by adjusting the number of VIV modes participating in the responses. When a large number of modes compete, the dominating frequency of cross-flow and in-line may change in time. For the Hanøytangen test, especially the time variation of the in-line frequency was much more pronounced than for the other tests (Larsen et al., 2012; Kim et al., 2021). Therefore, the in-line synchronization range of the new load model needed to be wider than for the VIV analysis of short and rigid pipes, and this could be achieved by controlling the in-line synchronization parameters.

To compare the performance of the new load model as a function of the in-line synchronization parameters, two empirical parameter sets were proposed. For the first one, all in-line synchronization parameters had values that were twice those of the corresponding cross-flow parameters. As a result, the in-line frequency was about twice the cross-flow frequency, which coincides with the combined cross-flow and in-line vibration tests by Dahl et al. (2010), and it is referred to as the New1 model or narrow-band synchronization (NB). For the second one, the non-dimensional frequency of the in-line was set to between 0.1 and 0.7, and the maximum energy transfer would occur when the non-dimensional frequency of the in-line was 0.5. The parameters were estimated based on the results of the pure in-line response tests (Aronsen, 2007; Ulveseter et al., 2017), and it is referred to as the New2 model or the wide-band synchronization model (WB). The previous model in Eq. (4) was also considered in order to compare with the new load model prediction performance (referred to as Prev). The same C_D, C_M, $C_{v,y}$, and $C_{v,x}$ which were optimized by Ulveseter et al. (2018) were applied for all cases. The empirical parameters of each load model are summarized in Table 4.

5. Comparison of the in-line load models based on simplified riser model

The performance of the new load model was evaluated with respect to response levels and frequency prediction. To focus on the load model performance only, the simplified riser model was applied. Also, the cases of high pretension were considered since this causes the interval between adjacent eigenfrequencies to become more narrow when the pretension increases as defined in Eqs. (7) to (9). This implies that the dominating frequency can be shifted easily into adjacent eigenfrequencies resulting in a wider synchronization range. Three test set-ups were selected among the high tension cases, and these comprise the lowest, middle, and highest current speeds (U = 0.38 m/s, 1.14 m/s, 1.96 m/s). The Prev., New1, and New2 load models were applied as basis for the time domain simulations.

5.1. Prediction of the synchronization range and dominating frequency

Wavelet analysis was applied in order to compare the frequency predictions. The x-axis, y-axis, and the colormap of each wavelet represent the time, frequency, and strain PSD. Wavelets were plotted for the cross-flow and in-line according to the current speed in Fig. 6. Each figure included the test and simulation wavelets at three different locations. These locations corresponded to the non-dimensional coordinates z/L = 0.03, z/L = 0.33, and z/L = 0.93, where L is the riser length and z starts from the top of the riser. The z/L = 0.33 was the location where the maximum stress was observed. Although the colormap scale of each plot was different from each other, the main comparisons were the dominating frequency and change of the colormap in time. The cross-flow and in-line results for the tests included the effect of the VIV but also external loads, which should be kept in mind as basis for the comparison.

As seen in Figs. 6a, 6c, and 6e, the dominating frequencies of the cross-flow showed a good correlation with respect to the measurements regardless of current speed, locations, and in-line load models. However, the frequency variation of the cross-flow in time, i.e. time-sharing process, were different from each other, which is likely to be related to different in-line responses between the Prev., New1, and New2 models. With respect to the in-line frequency predictions, seen in Figs. 6b, 6d, and 6f, different frequency predictions were observed between the in-line load models. The time-sharing processes and dominating frequency of Prev. were well predicted relative to the test results only for the lowest current speed (in Fig. 6b). The time-sharing was getting irregular as the current speed increased as seen in Figs. 6d and 6e. On the other hand, the time-sharing processes of the in-line of the New1 and New2 models were regular regardless of the locations and current speeds. However, the in-line synchronization ranges of New2 model were wider than that of New1 model and more similar to the test results. In terms of the dominating frequency, New1 gave better predictions than the New2 model for the low current velocity as seen in Fig. 6b. However, when the current speed increased, the in-line dominating frequency of New2 model was more accurate than for New1 model. Another difference in in-line predictions between New1 model and New2 model was that the results of New1 showed the space-sharing process. Near the bottom of the riser (z/L = 0.93), the in-line vibration synchronized not only with the high frequencies but also with the low frequencies due to the low current speed which also was observed in the test. The results of New2 model showed weaker space-sharing processes than those for New1 model.

For the previous load model, the in-line response was somewhat unstable and random because of its dependency on the cross-flow synchronization. However, this lacking stability of the in-line response was improved by introducing the independent in-line synchronization, and it was also able to describe different in-line response characteristics. In terms of the in-line synchronization parameters, New2 model fits the test results well with respect to the dominating frequency prediction and time-sharing process. However, the prediction accuracy was lower than for the New1 model in the low velocity range, and the space-sharing process of New1 model was more realistic.

5.2. Stress and response characteristics of the new load model

For the stress comparisons between New1 and New2 models, the standard deviations (STD)s of stress were calculated from the simulation for three different current speed cases. The STDs of stress induced by the cross-flow and in-line bending moments were calculated at every cross-section, and STDs of stress were plotted along the riser length in Fig. 7.

There were no significant differences in the cross-flow results between New1 and New2 models regardless of the current speed as seen in Figs. 7a, 7c, and 7e. On the other hand, there were significant differences for the in-line stress results for all the cases with different

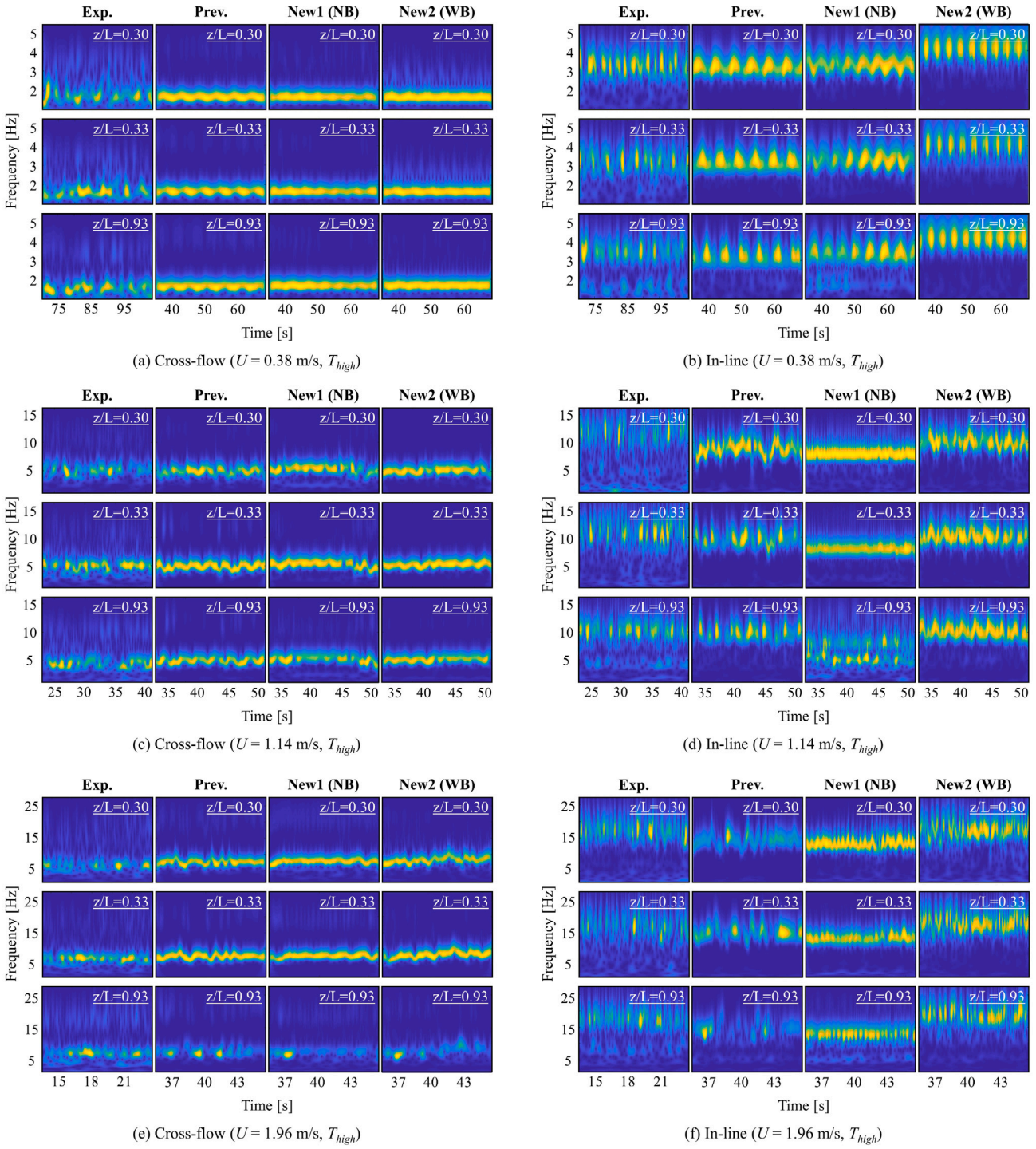

Fig. 6. Strain PSD wavelets for experiments and simulations using the simplified riser model. (For interpretation of the references to color in this figure legend, the reader is referred to the web version of this article.)

current magnitudes, and the differences between the stress profiles were observed from the point where the maximum stress occurred (z/L is about 0.3) to the bottom end of the riser as shown in Figs. 7b, 7d, and 7f. Because of the higher in-line mode order for New2 model than that of New1 model, the in-line stresses of New2 model were normally higher. Also, as discussed in the previous section, the space-sharing process of New1 model was more dominant than for New2 model near the bottom of the riser. This implies that New1 model was partially synchronized with the lower mode near the bottom end of the riser, which might result in low stresses.

To illustrate the response characteristics depending on the parameter sets, the trajectories of the VIV motion for the lowest current speed are illustrated along the riser length in Fig. 8. The cross-flow and in-line responses were non-dimensionalized with the diameter of the riser. As seen in Fig. 8, the amplitude differences were not significant between New1 and New2 models except the in-line amplitude at the lower part of the riser. However, the stability features of the response was different. The trajectories of New1 model were more stable and varied along the riser while the results of New2 model showed chaotic responses.

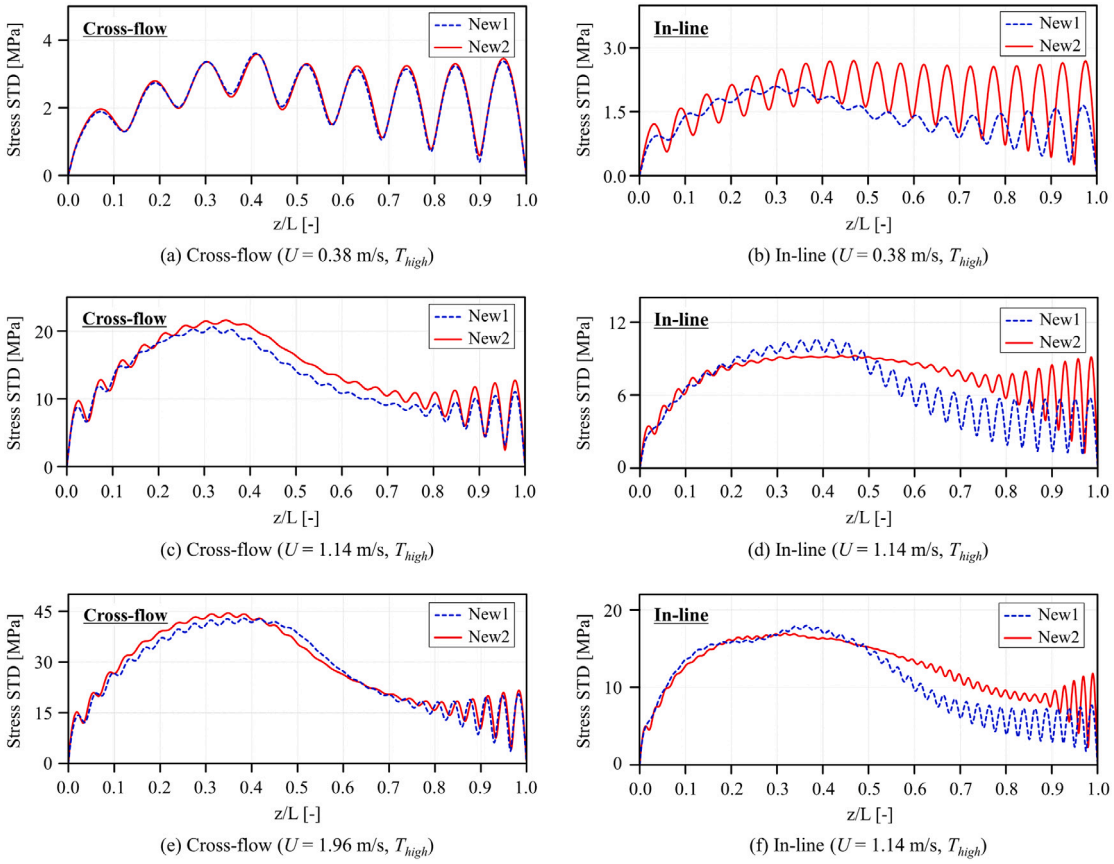

Fig. 7. The stress STD along the riser length for the New1 and New2 models.

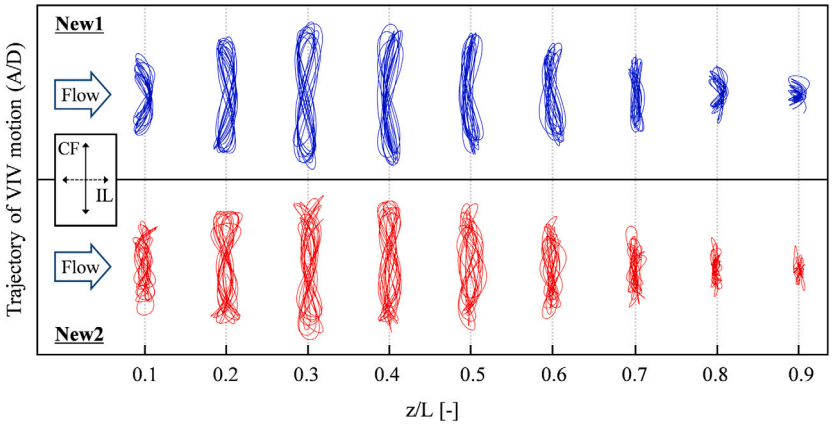

Fig. 8. Trajectory of VIV for New1 and New2 models along the riser length (U = 0.38 m/s, T_{high}).

In summary, the in-line response of the Hanøytangen test showed a wide range of time-sharing processes and unstable response due to the mode competition. Considering the results in Figs. 6 to 8, New2 model was found appropriate to describe the unstable VIV response of the Hanøytangen test. In the following sections, the New2 model was applied for all the time domain VIV simulations. The simulations with the simplified riser model are referred to as TD_S, while TD_A hereafter refers to the advanced riser model.

6. VIV induced axial vibrations

As discussed in Section 2.2, tension fluctuations were observed at the top of the riser for all the tests, and the magnitude of the tension variation increased for increasing towing speeds. Tension fluctuations are illustrated in relation to the riser configurations in Fig. 9.

The riser in the flow is sagging due to the drag force relative to the initial configuration in Fig. 9a, as shown in Figs. 9b and 9c. Correspondingly, the riser oscillates twice (i.e. runs through two periods) in the vertical direction during one period of cross-flow (ω) and in-line (2ω) oscillation. The frequencies of axial vibrations are 2ω (induced by the cross-flow vibrations) and twice that for the in-line, i.e 4ω (induced by the in-line vibration). Therefore, the capabilities of the advanced riser model TD_A with respect to capturing such behavior are investigated in the following.

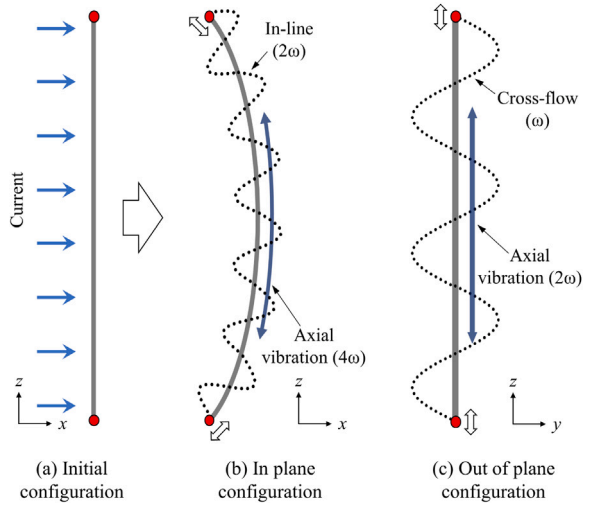

Fig. 9. Illustration of axial vibrations caused by in-line and cross-flow excitations.

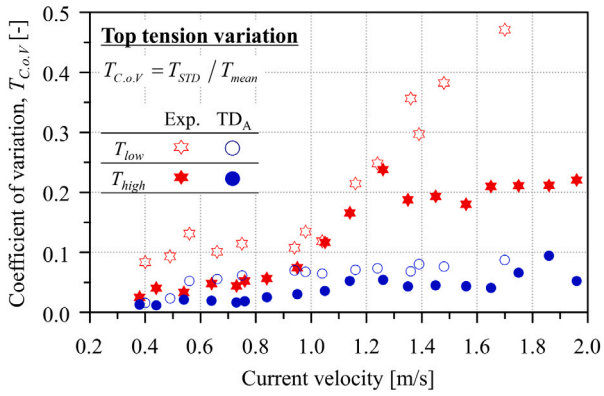

Fig. 10. C.o.V of the tension at the top of the riser (tests and simulations).

6.1. Axial non-resonant vibrations caused by VIV

Most of the tension fluctuations observed in the test and simulations where axial non-resonant vibrations, i.e. vibrations with a frequency outside the first axial vibration mode. To quantify the top tension fluctuations statistically, the Coefficient of Variation of the top tension ($T_{C.o.V} = T_{STD}/T_{mean}$) for TD_A and for the test are plotted in Fig. 10. As shown in Fig. 10, the results for the cases with low tension, T_{low} were higher than those for the cases with high tension, T_{high} both for the tests and the TD_A. The low pretension decreased the system stiffness, which allowed more tension fluctuation. Also, the results of the test were amplified as the current speed increased regardless of tension magnitudes. The axial vibrations induced by the cross-flow are normally much higher than those induced by the in-line since the magnitude of the axial vibrations is proportional to the square of amplitude. In the case of the TD_A, the results showed similar trends, however, the magnitude of the tension fluctuations were seen to be significantly lower than for the tests.

These differences might be related to the structural- or the hydrodynamic damping. VIV response is more affected by hydrodynamic damping in the present study as the structural damping was low, refer to Section 3.2. The hydrodynamic damping force can be controlled by means of the drag coefficient, C_D or the vortex shedding forces, $C_{v,x}$ and $C_{v,y}$, refer to Eq. (1). The sensitivities of tension fluctuations to the drag coefficients, C_D were investigated in order to throw light on this effect. The results are plotted for the low- and high-current speed cases in Fig. 11. From the results in this figure, the tension fluctuations of TD_A for both current speeds were getting similar to the test as the drag coefficient decreased. However, the lower drag coefficient than the proposed one allowed for large VIV response and axial vibration. The cross-flow and in-line vortex shedding force of the load model are correlated with the drag force term. The drag force term in Eq. (1) leads to a smaller force due to the reduced C_D value. As a consequence of the decreased damping force, both the in-line and cross-flow response amplitude and vortex shedding force will be amplified. Then, the total force in the in-line direction increases due to the higher projected vortex shedding force (i.e. the increase of effective diameter). In short, the decrease of the drag coefficient does not necessarily mean a reduction of the total hydrodynamic damping. The drag coefficient of the load model was set to be 1.2, which was based on fixed cylinder test data (Thorsen et al., 2017), however, the sensitivity analysis results suggested that the drag coefficient of flexible pipes could be smaller than 1.2.

Other uncertainties in the structural model may also contribute to the discrepancy, e.g., there was no frictional force included in the pulley system, and the vessel movement in the vertical direction was constrained, hence excluding the effect of towing vessel mass and hydro-static stiffness. Therefore, rather than optimizing the empirical coefficients in the load model in order to agree as well as possible with the test results, it was instead focused upon whether the tension fluctuation was captured by the simulations and how these were correlated to the overall VIV response. To compare the frequency of tension fluctuations between the test and the TD_A, wavelet analysis was applied for both the tension and strain time series. The low- and high current speed results are illustrated in Fig. 12.

Figs. 12a and 12b include the top tension- (z/L = 0.00) and the strain wavelets for two different in-line and cross-flow cases near the top end (z/L = 0.03) and the point where maximum stress observed (z/L = 0.33). The scales of the wavelets are different from each other, however, the correlation between the strains and the tension variations is clearly observed both for the tests and the TD_A. For the low current speed in Fig. 12a, the frequency of the tension is about twice that of the in-line strain, and its pattern is similar to the in-line strains patterns at z/L = 0.03 for both the test and the TD_A. For the case of the high current speed in Fig. 12b, the results were similar to those for the low current speed case, but the tension was dominated by the cross-flow response. The frequency variation and the dominating frequency were well predicted by the TD_A. Furthermore, the frequency variations of the in-line and cross-flow strains were similar to each other at two points (z/L = 0.03 and z/L = 0.33) for both the test and the TD_A. This implies that the tension fluctuations affect the VIV response not only near the top but also at other locations.

6.2. Axial resonant vibrations induced by the cross-flow motion

The axial resonant vibration occurs when the VIV frequency coincides with the first mode of vibration in the axial direction of the riser. Resonance could be induced by both cross-flow and in-line effects, but it was found that the cross-flow induced resonance was the most severe. For a steel riser, the cross-flow induced axial resonant vibration occurs when the current speed reaches the critical velocity formulated as below (Huse, 1999).

$$V_c = \frac{c D_e}{8\, St\, L} \tag{10}$$

where, the V_c is the critical velocity, and c is the velocity of sound in steel (5130 m/s). For the Hanøytangen riser, the V_c is about 1.26 m/s when St is 0.17.

The equation was derived by assuming that the VIV is high- and single-mode in uniform flow conditions, however, the dominating mode may vary in a sheared current. Due to the competition among the modes, the axial resonant vibration could occur intermittently only when certain conditions are satisfied. For the TD_A, the cross-flow was relatively stationary, which caused axial resonance for the two cases to

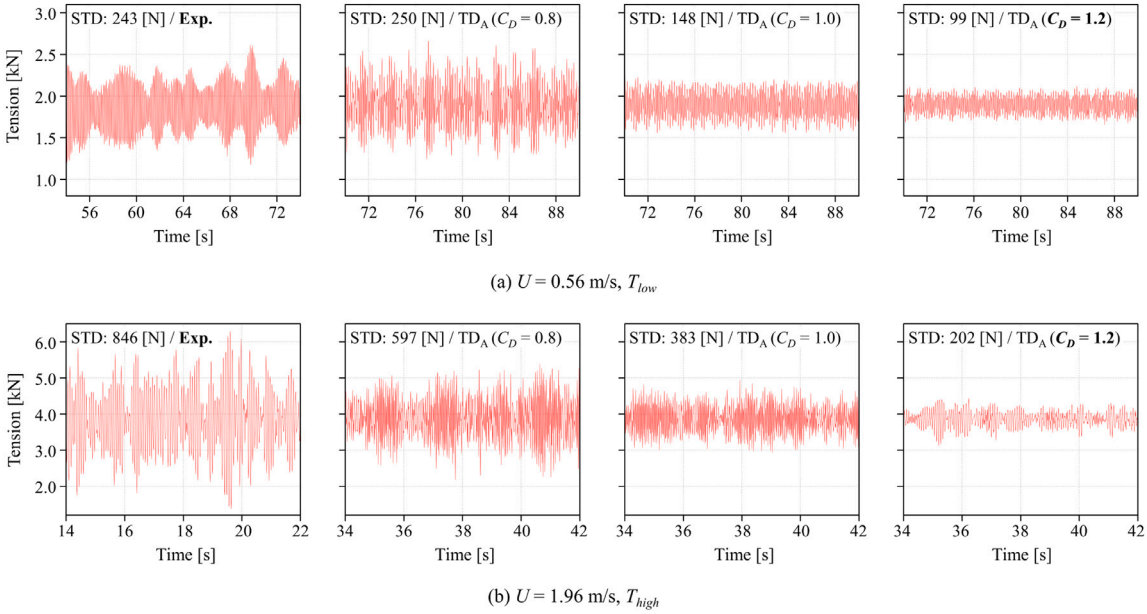

Fig. 11. Tension fluctuation sensitivities to the drag coefficients.

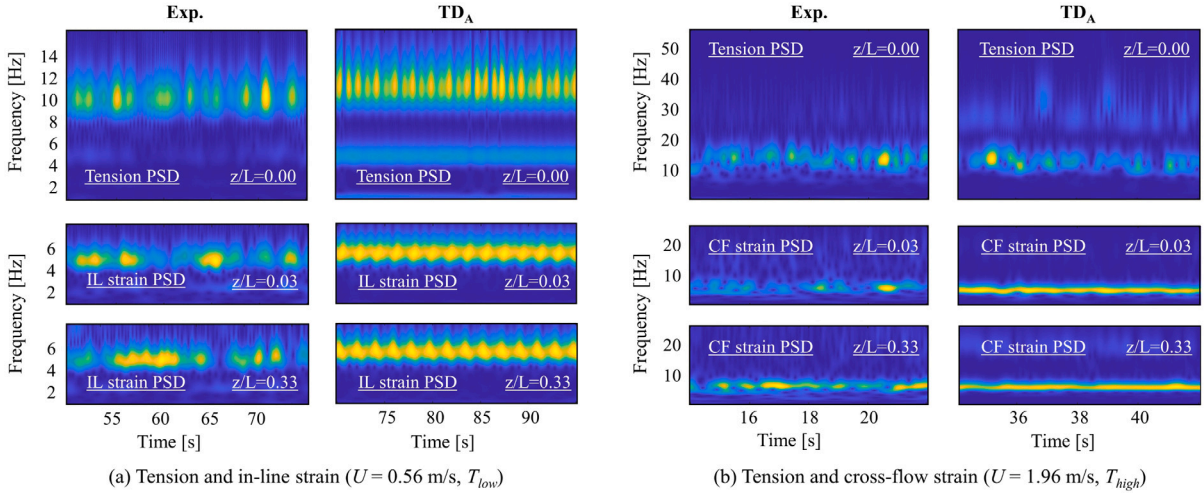

Fig. 12. Tension PSD and strain PSD Wavelet analysis for three different locations. (For interpretation of the references to color in this figure legend, the reader is referred to the web version of this article.)

take place at the respective frequency which corresponded most to the critical velocity. One of the cases (i.e. the high-velocity, high-tension case) and the corresponding results from the test are analyzed in more detail in Fig. 13.

The first row of Figs. 13a and 13b represents the tension signal at the top, and the second row contains the wavelet for the tension PSD. The last row shows the contour of cross-flow bending moment in time. As observed from Fig. 13b, the tension in the simulation gradually increased from 37.4 s and increased rapidly at 38.2 s When resonance is observed, the cross-flow bending moment significantly decreases not only near the top but also at the other locations. This was referred to as to the feedback effect (Huse, 1998), and might be due to the combination of an increase of dynamic stiffness and unstable VIV response. Regarding the results from the test, it was assumed that axial resonant vibrations were not fully developed as observed from Fig. 13a.

In order to compare the decrease of the stress due to the feedback effect, the STDs of the cross-flow induced stresses are plotted along the riser length. The results in Fig. 14a correspond to a lower current speed case with axial non-resonant vibration. Furthermore, the results in Fig. 14b correspond to a high current speed with axial resonant vibration taking place in the TD_A simulation. In Fig. 14b, an additional result of TD_A using a short time window where axial resonance is observed (38s–39s) is included. When the current speed increases, it is expected that the stress levels will increase, which is observed for the test results. However, the STD of the stress for the TD_A simulation (blue line) is found to decrease somewhat as shown in Fig. 14b compared to that in Fig. 14a. This is due to the axial resonance, and when this occurs, the stress near the top increases but the stress level at other locations decreases as seen from the black dot line in Fig. 14b. It should also be kept in mind that the axial resonant vibration caused by in-line effects was excluded from the discussion due to its relatively small magnitude. However, both for the tests and for the simulations axial vibration induced by in-line effects can occur, which can also influence the VIV response. However, the TD_A capability of describing the axial resonance behavior observed in the test has been clearly demonstrated, and as such represents a significant step forward with respect to VIV modeling practice.

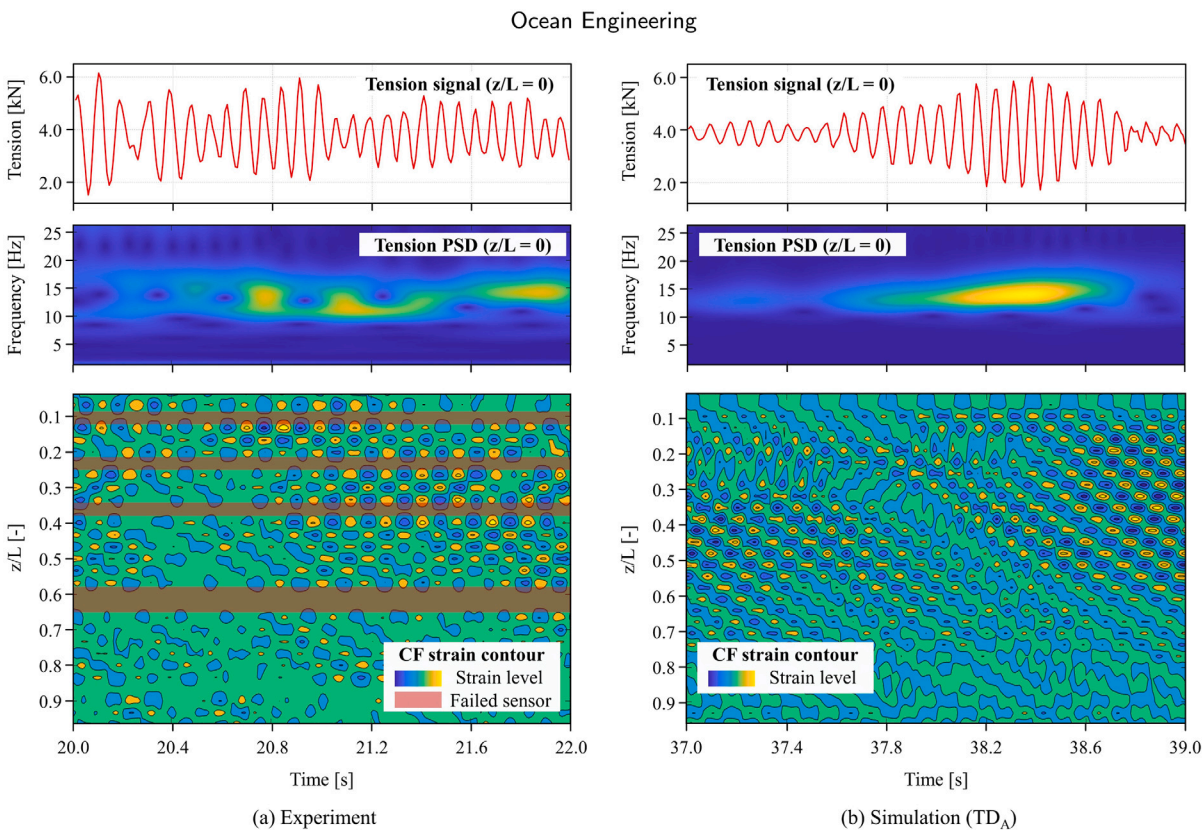

Fig. 13. Top tension and cross-flow strain analysis (U = 1.86 m/s, T_{high}). (For interpretation of the references to color in this figure legend, the reader is referred to the web version of this article.)

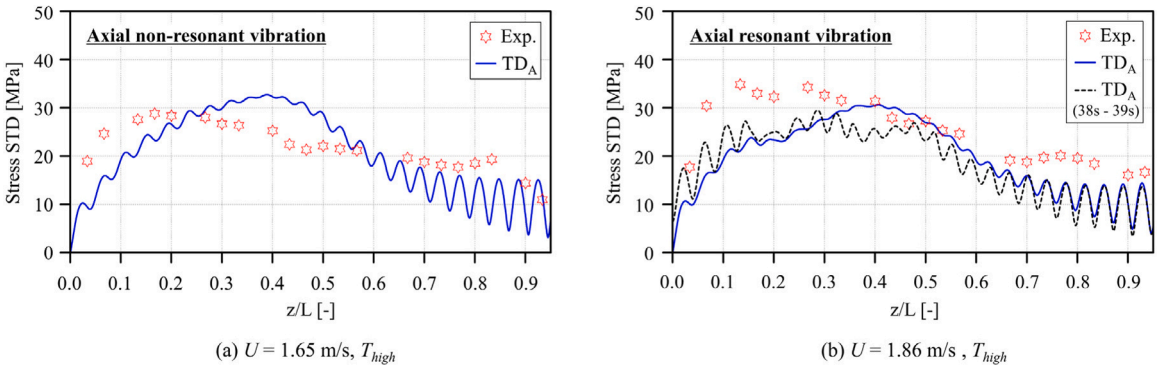

Fig. 14. STD of the cross-flow stress along the riser for both axial non-resonant and axial resonant vibrations.

7. Validation of the new load model

In this section, the prediction performance of the new load model is evaluated, and differences of VIV predictions depending on the riser modeling choices discussed.

7.1. Differences of top tension between riser models

To investigate the differences between TD_S and TD_A related to boundary conditions, the percentwise errors in Eq. (11) were plotted as a function of current velocity in Fig. 15.

$$T_{error} = \left| \frac{T_{mean,\mathrm{Sim.}} - T_{mean,\mathrm{Exp.}}}{T_{mean,\mathrm{Exp.}}} \right| \times 100\ \% \tag{11}$$

It is seen that the errors of TD_S become larger when the current speed increases, which is due to the top tension increase from the drag forces. In order to obtain a similar top tension in the TD_S simulation to that for the tests, the initial tension should be set to a level that reflected the drag force effect, but no such optimization was performed. However, by analyzing the results obtained by the TD_A simulations, it was seen that the relative errors were about 1%–2% regardless of the current and tension level. This implies that TD_A corresponds to a better riser modeling approach in order to represent the features of the tests.

7.2. Stress and frequency predictions

For the stress comparisons, the maximum standard deviation of the VIV induced stress at each cross-section was averaged along the riser length. The results of TD_S and TD_A are compared in Fig. 16 both for the cross-flow and in-line cases. The area below the diagonal line in Figs. 16a and 16b indicates which cases that give predictions that are lower than for the tests, and the area above the diagonal

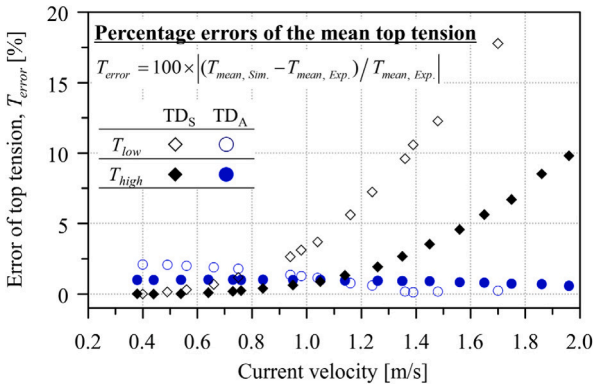

Fig. 15. Mean of the tension at the top of the riser (simulations).

corresponds to overprediction. Generally, tests and both simulations showed good correlations, however, the TD_S tends to overestimate more than TD_A for both the cross-flow and the in-line cases. The higher pretension of TD_S increased the eigenfrequency of the riser and resulted in higher mode VIV. In addition, the tension fluctuations of TD_A gave rise to energy transfer in the axial direction of the riser. As seen in Fig. 16a, two cases of TD_A showed much lower stress results due to axial resonant vibrations.

When it comes to frequency prediction, the peak frequency of the strain PSD was defined as the dominating frequencies, and the dominating frequency at z/L = 0.33 were compared to each other. Comparisons were made in the same way as for the mean STD stress comparison provided by Fig. 17. Overall, the results of TD_S were more conservative than TD_A because of the higher pretension and showed a good correlation with the test for both cross-flow and in-line. However, it was difficult to conclude on the prediction accuracy due to the uncertainty of the empirical parameters as discussed in Section 6. Furthermore, the in-line results of TD_S and TD_A in Fig. 17b were more scattered than those for the cross-flow. To gain insights on the VIV frequency along the riser, the wavelets of the strains were compared for all methods at three different locations. The most tension dominated cases and bending stiffness dominated cases were selected, and results are shown in Fig. 18.

In the case of the VIV synchronization at low current speed as shown in Figs. 18a and 18b, the synchronization ranges of TD_S and TD_A were similar to the test regardless of the locations. However, for the bending stiffness dominated case in Figs. 18c and 18d, the frequency variation patterns of both TD_S and TD_A became irregular due to the instability of the VIV response. Furthermore, in the case of TD_S, there were no significant differences in frequency characteristics according to the locations. However, as shown in Figs. 18c and 18d, the results for the TD_A near the top displayed some irregularities due to tension fluctuations, and a weak space sharing was also observed near the bottom. In short, although the results in Fig. 17 shows that TD_S gave better frequency predictions than TD_A, the TD_A reflects the characteristics of the tests better. The time- and space-sharing could be simulated simultaneously by application of the new in-line load model combined with the TD_A, which was able to reflect the test characteristics more adequately.

7.3. Fatigue damage predictions

In order to compare the fatigue damage, the maximum fatigue damage around the circumference at each cross-section was plotted along the riser in Fig. 19. The fatigue damage was calculated using the bending stresses, and the rainflow counting method which is implemented in the WAFO MATLAB toolbox (Brodtkorb et al., 2000) was applied. The material constant, log$a$ was 11.687, and the slope of the S–N curve, k was 3 (Baarholm et al., 2006). The results in Fig. 19 comprise a total of 6 cases that are distinguished by the tension levels and current speeds.

When it comes to the overall trends, the high pretension results from the TD_A simulation in Figs. 19b, 19c, and 19d are relatively more irregular than the results of the low pretension cases in Figs. 19a, 19c, and 19e. This was related to the number of modes participating in VIV response as discussed in Section 5. On the other hand, in the case of TD_S, all cases showed a stable fatigue damage profile. A possible explanation is that the VIV responses at each cross-section were not coupled with the response of the other cross-section. Furthermore, the differences in the mode shape and the location of maximum fatigue damage between TD_S and TD_A were observed as seen in Fig. 19c, which showed a more stable profile than other cases.

Comparing the results in terms of the current speed, for the low current speed when the in-line is relatively dominant, the prediction of TD_A showed better performance than that of TD_S as seen in Figs. 19a and 19b. Especially, for the high tension cases, although there was inconsistency in the lower part of the riser due to weak space-sharing processes, the irregularity of the profile was well predicted. For the middle current speeds, the dominance of the cross-flow of the response is getting increased so that both in-line and cross-flow effects are important. The axial non-resonant vibration by both responses made the stability of response worse. Therefore, the fatigue damages of the

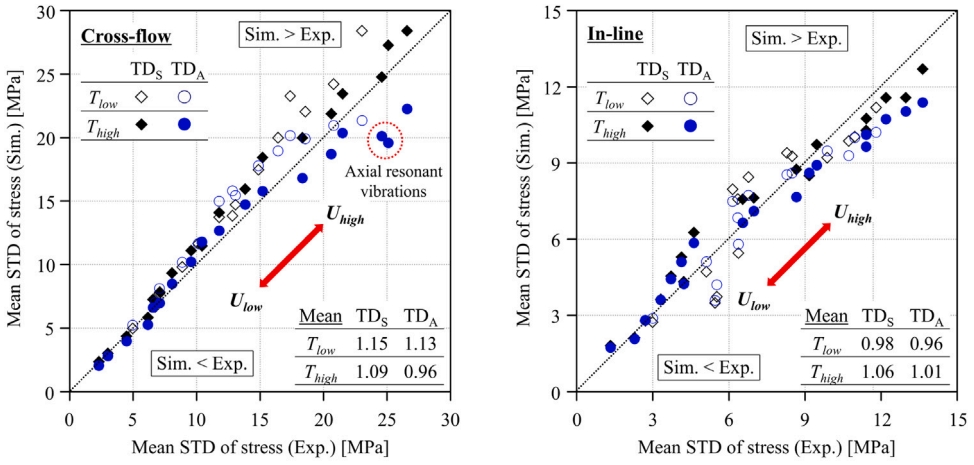

(a) Cross-flow (b) In-line

Fig. 16. Comparison of the mean STD of the stresses.

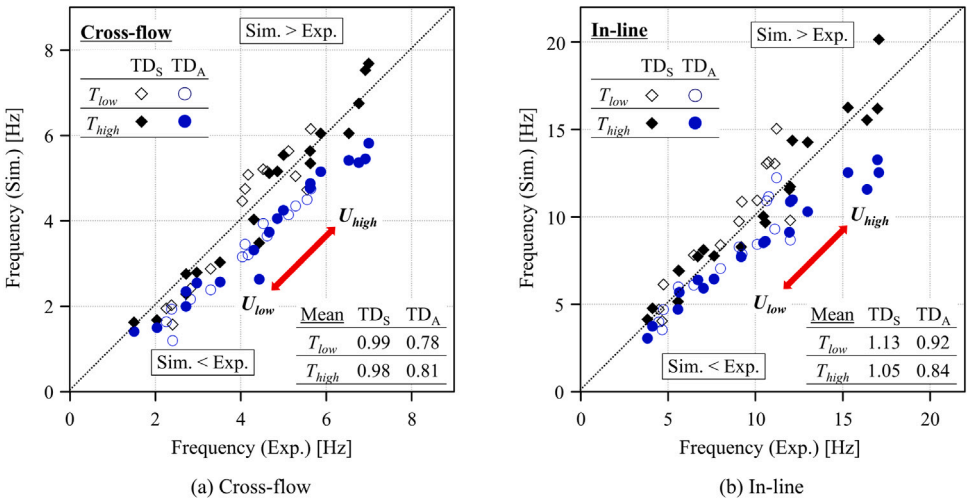

Fig. 17. Comparison of the dominating frequencies at the z/L = 0.33.

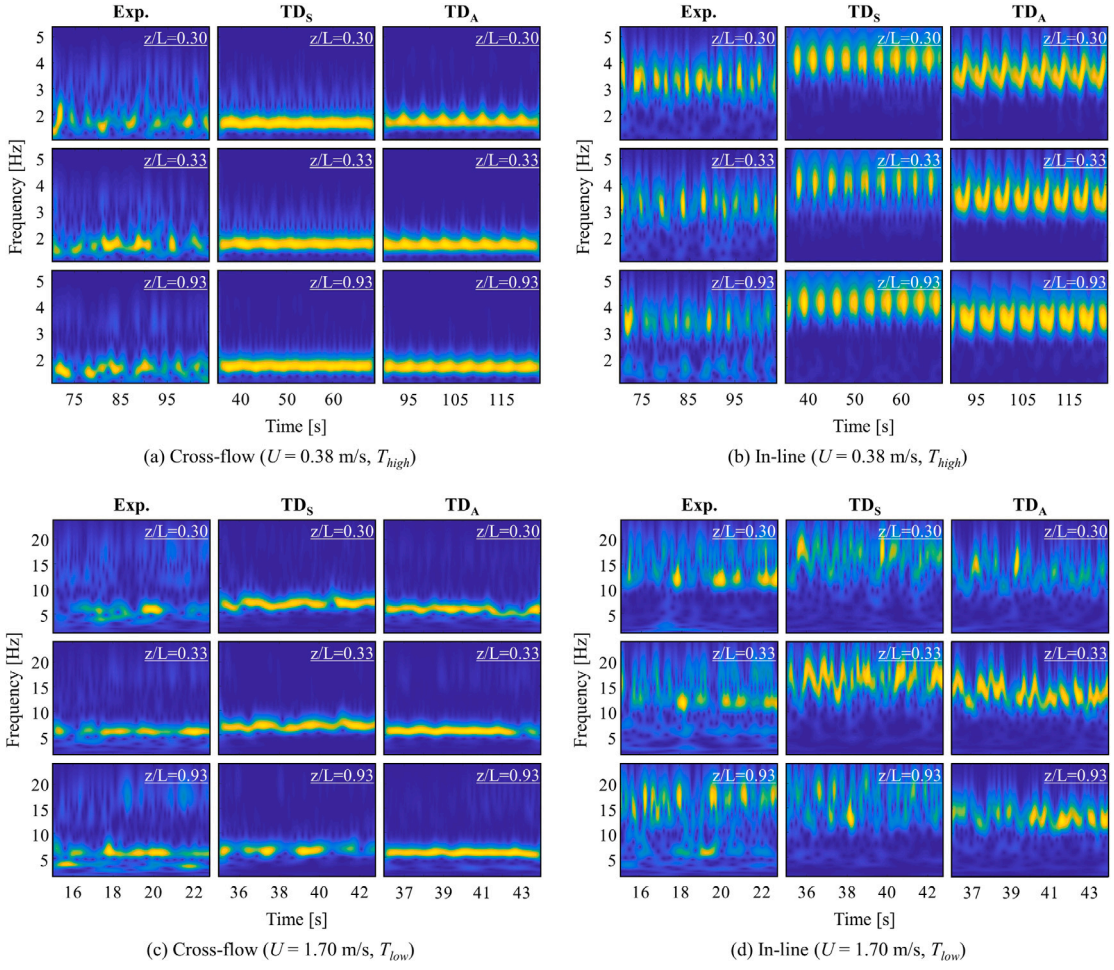

Fig. 18. Comparison of strain PSD wavelets. (For interpretation of the references to color in this figure legend, the reader is referred to the web version of this article.)

test were more evenly distributed along the riser than in low- and high-current speed cases as seen in Figs. 19c and 19d. This means that the prediction accuracy of TD_A for the middle current speed will be lower than for the other current speed cases. In the case of high current speed, when the cross-flow was dominant, TD_S was found to be conservative, while TD_A showed good correlation with the test results as seen in Figs. 19e and 19f.

In order to evaluate the fatigue damages for all cases, the mean value of the fatigue along the whole riser was compared for the tests versus the simulations, and a corresponding bias factor was defined, i.e λ_{fat} ($= D_{mean,\,\mathrm{Sim.}}/D_{mean,\,\mathrm{Exp.}}$). Here, $D_{mean,\,\mathrm{Exp.}}$ is the average of the fatigue damage at each sensor, and $D_{mean,\,\mathrm{Sim.}}$ is the fatigue damage at the sensor locations which is estimated based on the results from the simulations. The bias factor, λ_{fat} is plotted as a function of current velocity according to the pretension level in Fig. 20. For low current

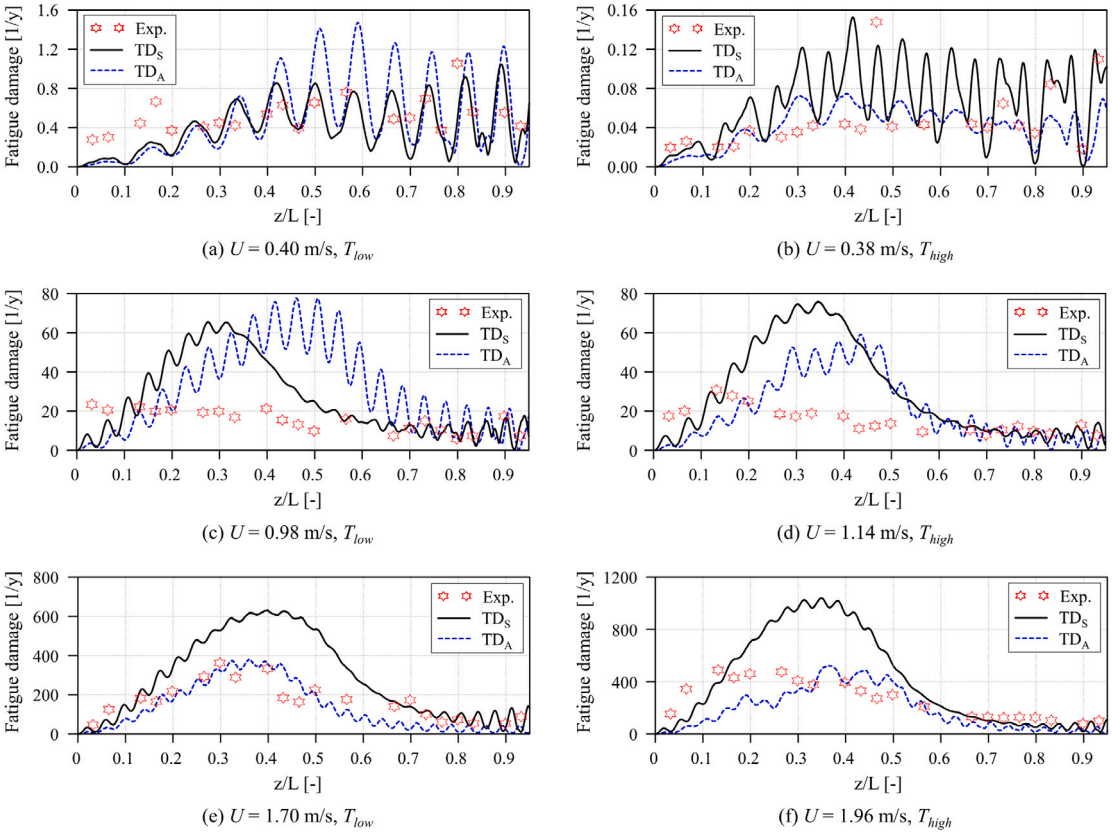

Fig. 19. Fatigue damage profiles for different currents and pretensions.

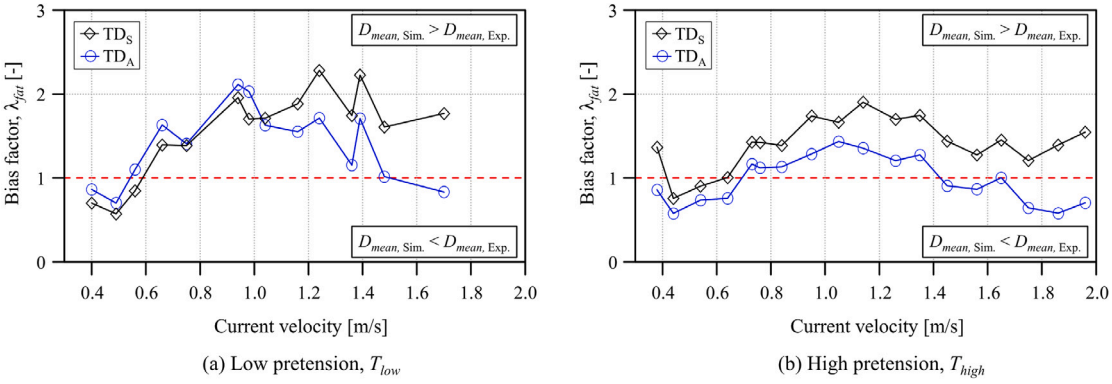

Fig. 20. Fatigue damage comparison in terms of the bias factor.

speeds, both the TD_S and the TD_A underpredict the fatigue damage, while for increasing speeds they both overpredict the damage. For the low tension cases as seen in Fig. 20a, the results from the TD_A simulations showed a good correlation with the results from the test with a bias factor of 2 or less, although the results for the intermediate current speeds are somewhat irregular. For the high tension cases, the TD_A gives even better predictions than for low tension as seen from Fig. 20b. Although the results in Fig. 20 only includes a comparison of the average fatigue damage, the corresponding results in terms of the ratio between the values of the maximum fatigue damage is less than 4. Regarding results from the TD_S simulations, the bias factor is somewhat higher than for the TD_A in the case of high pretension. For low pretension the bias factor is smaller than for TD_A for current velocities up to around 1.0, while above this value the ratio becomes higher than for TD_A.

8. Conclusions

In the present study, numerical simulations of the Hanøytangen tests were performed in order to develop an improved time-domain VIV model that is suitable for the estimation of deepwater riser VIV. The main characteristics of the Hanøytangen tests related to VIV corresponded to a high-mode VIV response, bending stiffness dominated behavior, and sheared current. When it comes to the prediction performance of the new load model, the following notable results were obtained:

- The improved in-line synchronization concept is found to be reasonable in term of dominating frequency and time-sharing prediction, and it is found to be more robust with respect to modeling the in-line response characteristics than the previous load model.

- The improved load model with narrow synchronization bandwidth (New1) gave a good prediction of the frequency at low current speeds and showed good performance with respect to representation of the space-sharing process. On the other hand, the load model with wide synchronization bandwidth (New2) gave good predictions of the frequency and a good representation of the time-sharing process for the higher current speeds.
- The New2 model is found to be favorable with respect to predicting deepwater riser VIV responses characterized by a wide in-line vibration frequency variation range due to the high mode VIV and the sheared current.

In addition, a comparison was made of the VIV predictions based on the simplified (linear) and advanced (non-linear) riser models. The advanced riser model increased the VIV prediction accuracy by capturing the main non-linear effects inherent in the test due to tension fluctuations. The insights based on the tension fluctuations can be summarized as:

- The axial non-resonant vibrations could be adequately simulated by the new load models. Although the degree of tension variations was quite different from the test, the frequency characteristics of the tension variations were well predicted.
- The tension fluctuation differences between tests and simulations seem to be related to the magnitude of VIV responses. The hydrodynamic damping is one of the contributing parameters to be further investigated.
- Resonant axial vibrations were observed in the simulation, and it was observed that the VIV response possibly decreases when axial resonant vibration occurs.
- The tension fluctuations affect the stability of the VIV process and thereby the prediction uncertainties along the riser. Therefore, non-linear time domain analysis needs to be considered for riser systems with large tension fluctuations.

From the present study, it was demonstrated that not only good quality of the VIV prediction model itself but also accurate structural modeling is required in order to achieve precise estimates and explain the inherent physics. The proposed load model was found capable of capturing the key characteristics of the deepwater riser subjected to high mode VIV responses. However, there are still uncertainties related to prediction accuracy, especially with respect to hydrodynamic damping and other load coefficients. The uncertainties associated with these empirical parameters need to be reduced by means of additional correlation studies based on suitable test data.

CRediT authorship contribution statement

Sang Woo Kim: Conceptualization, Methodology, Software, Formal analysis, Investigation, Data curation, Writing – original draft & editing, Writing – review & editing, Visualization, Validation. **Svein Sævik:** Conceptualization, Methodology, Software, Validation, Investigation, Writing – original draft & editing, Writing – review & editing, Supervision, Project administration. **Jie Wu:** Conceptualization, Methodology, Validation, Investigation, Resources, Writing – original draft & editing, Writing – review & editing, Supervision, Project administration. **Bernt Johan Leira:** Methodology, Validation, Investigation, Writing – original draft & editing, Writing – review & editing, Supervision, Project administration.

Declaration of competing interest

The authors declare that they have no known competing financial interests or personal relationships that could have appeared to influence the work reported in this paper.

Acknowledgments

The authors wish to thank the Norwegian Deepwater Programme for allowing the use of the Hanøytangen experiments, and SINTEF Ocean for providing the data. We would also like to thank Mr. Halvor Lie, Dr. Elizabeth Passano, Dr. Decao Yin, and Prof. Emeritus Carl M. Larsen for contributing with valuable discussions on VIV in general.

References

Aronsen, K.H., 2007. An Experimental Investigation of In-line and Combined In-line and Cross Flow Vortex Induced Vibrations (Ph.D. thesis). Norwegian University of Science and Technology, Trondheim, Norway.
Baarholm, G.S., Larsen, C.M., Lie, H., 2006. On fatigue damage accumulation from in-line and cross-flow vortex-induced vibrations on risers. J. Fluids Struct. 22(1), 109–127.
Baker, W.E., Cox, P.A., Westine, P.S., Kulesz, J.J., Strehlow, R.A., 1983. Explosion Hazards and Evaluation. Elsevier Scientific Publishing Company, New York.
Braaten, H., Lie, H., 2005. NDP Riser High Mode VIV Tests Main Report. Technical Report, Norwegian Marine Technology Research Institute, Trondheim, Norway.
Brodtkorb, P.A., Johannesson, P., Lindgren, G., Rychlik, I., Rydén, J., Sjö, E., 2000. Wafo - A matlab toolbox for analysis of random waves and loads. International Offshore and Polar Engineering Conference, ISOPE-I-00-264.
Dahl, J.M., Hover, F.S., Triantafyllou, M.S., Oakley, O.H., 2010. Dual resonance in vortex-induced vibrations at subcritical and supercritical Reynolds numbers. J. Fluid Mech. 643, 395–424.
DNV.GL, 2017. Recommended Practice-F204: Riser Fatigue. Technical Report, Det Norske Veritas and Germanischer Lloyd, Oslo, Norway.
Drengsrud, H., 2019. Systematic Evaluation of VIV Prediction for Riser with Partial Strake Coverage (Master's Thesis). Norwegian University of Science and Technology, Trondheim, Norway.
Facchinetti, M.L., Langre, E.d., Biolley, F., 2004. Coupling of structure and wake oscillators in vortex-induced vibrations. J. Fluids Struct. 19 (2), 123–140.
Gabbai, R.D., Benaroya, H., 2005. An overview of modeling and experiments of vortex-induced vibration of circular cylinders. J. Sound Vib. 282(3), 575–616.
Huse, E., 1997. Large scale testing of riser models, main report.
Huse, E., 1998. VIV induced tension fluctuations in deep sea steel risers.
Huse, E., 1999. Investigation of axial vibrations in deep sea risers using a truncated riser model.
Huse, E., Kleiven, G., Nielsen, F., 1999. VIV-induced axial vibrations in deep sea risers. Offshore Technology Conference, Paper NO. OTC-10932-MS.
Kim, S.W., Sævik, S., Wu, J., Leira, B.J., 2021. Simulating high-mode vortex-induced vibration of a riser in linearly sheared current using an empirical time-domain model. J. Offshore Mech. Arct. Eng. 143(4).
Larsen, C.M., Lie, H., Passano, E., Yttervik, R., Wu, J., Baarholm, G.S., 2017. VIVANA-Theory Manual, 4.10.1.. SINTEF Ocean, Trondheim, Norway.
Larsen, C.M., Zhao, Z., Lie, H., 2012. Frequency components of vortex induced vibrations in sheared current. ASME Paper No. OMAE2012-83092.
Lie, H., Kaasen, K.E., 2006. Modal analysis of measurements from a large-scale VIV model test of a riser in linearly sheared flow. J. Fluids Struct. 22(4), 557–575.
Ogink, R.H.M., Metrikine, A.V., 2010. A wake oscillator with frequency dependent coupling for the modeling of vortex-induced vibration. J. Sound Vib. 329 (26), 5452–5473.
Potts, A.E., Potts, D.A., Marcollo, H., Jayasinghe, K., 2018. Strouhal number for VIV excitation of long slender structures. ASME Paper No. OMAE2018-77433.
Sarpkaya, T., 2004. A critical review of the intrinsic nature of vortex-induced vibrations. J. Fluids Struct. 19(4), 389–447.
SINTEF Ocean, 2017a. RIFLEX 4.10.0 Theory Manual. Trondheim, Norway.
SINTEF Ocean, 2017b. SIMA 3.4 User Guide. Trondheim, Norway.
SINTEF Ocean, 2017c. SIMO 4.10.0 Theory Manual. Trondheim, Norway.
Srinil, N., Zanganeh, H., 2012. Modelling of coupled cross-flow/in-line vortex-induced vibrations using double duffing and van der pol oscillators. Ocean Eng. 53, 83–97.
Swithenbank, S.B., 2007. Dynamics of Long Flexible Cylinders at High-Mode Number in Uniform and Sheared Flows (Ph.D. thesis). Massachusetts Institute of Technology, Cambridge, MA, USA.
Thorsen, M.J., Sævik, S., Larsen, C.M., 2014. A simplified method for time domain simulation of cross-flow vortex-induced vibrations. J. Fluids Struct. 49, 135–148.
Thorsen, M.J., Sævik, S., Larsen, C.M., 2016. Time domain simulation of vortex-induced vibrations in stationary and oscillating flows. J. Fluids Struct. 61, 1–19.
Thorsen, M.J., Sævik, S., Larsen, C.M., 2017. Non-linear time domain analysis of cross-flow vortex-induced vibrations. Mar. Struct. 51, 134–151.
Triantafyllou, M., Triantafyllou, G., Tein, Y.S.D., Ambrose, B.D., 1999. Pragmatic riser VIV analysis. Offshore Technology Conference, Paper NO. OTC-10931-MS.
Trim, A.D., Braaten, H., Lie, H., Tognarelli, M., 2005. Experimental investigation of vortex-induced vibration of long marine risers. J. Fluids Struct. 21(3), 335–361.
Ulveseter, J.V., Sævik, S., Larsen, C.M., 2017. Time domain model for calculation of pure in-line vortex-induced vibrations. J. Fluids Struct. 68, 158–173.

Ulveseter, J.V., Thorsen, M.J., Sævik, S., Larsen, C.M., 2018. Time domain simulation of riser VIV in current and irregular waves. Mar. Struct. 60, 241–260.

Ulveseter, J.V., Thorsen, M.J., Sævik, S., Larsen, C.M., 2019. Simulating fundamental and higher harmonic VIV of slender structures. Appl. Ocean Res. 90.

Vandiver, J.K., Jaiswal, V., Jhingran, V., 2009. Insights on vortex-induced, traveling waves on long risers. J. Fluids Struct. 25(4), 641–653.

Vandiver, J.K., Li, L., 2005. SHEAR7 V4.4 Program Theoretical Manual. Department of Ocean Engineering, Massachusetts Institute of Technology, Cambridge, MA.

Vandiver, J.K., Swithenbank, S.B., Jaiswal, V., Jhingran, V., 2006. Fatigue damage from high mode number vortex-induced vibration. ASME Paper No. OMAE2006-92409.

Voie, P.E., Larsen, C.M., Wu, J., Resvanis, T., 2016. VIV BEST PRACTICE: Guideline on Analysis of Vortex-Induced Vibrations in Risers and Umbilicals. Technical Report, Det Norske Veritas and Germanischer Lloyd, Oslo, Norway.

Williamson, C.H.K., Govardhan, R., 2004. Vortex-induced vibrations. Annu. Rev. Fluid Mech. 36(1), 413–455.

Wu, J., Jin, j., Yin, D., Lie, H., Passano, E., Sævik, S., Tognarelli, M., Grytøyr, G., Andersen, T., Karunakaran, D., Igland, R., 2020a. Time domain VIV analysis tool VIVANA-TD: validations and improvements. ASME Paper No. OMAE2020-18759.

Wu, J., Yin, D., Lie, H., Larsen, C.M., Baarholm, R.J., Liapis, S., 2019. On the significance of the higher-order stress in riser vortex-induced vibrations responses. J. Offshore Mech. Arct. Eng. 141(1).

Wu, J., Yin, D., Lie, H., Riemer-Sørensen, S., Sævik, S., Triantafyllou, M., 2020b. Improved VIV response prediction using adaptive parameters and data clustering. J. Mar. Sci. Eng. 8(2), 127.

Xue, H., Wang, K., Tang, W., 2015. A practical approach to predicting cross-flow and in-line VIV response for deepwater risers. Appl. Ocean Res. 52, 92–101.

Yuan, Y., Xue, H., Tang, W., 2017. An improved time domain coupled model of cross-flow and in-line vortex-induced vibration for flexible risers. Ocean Eng. 136, 117–128.